Theoretical description of field-assisted postcollision interaction in Auger decay of atoms

S. Bauch* and M. Bonitz

Institut für Theoretische Physik und Astrophysik and Christian-Albrechts-Universität zu Kiel, D-24098 Kiel, Germany

(Received 23 March 2012; published 22 May 2012)

In a recent publication [Schütte *et al.*, Phys. Rev. Lett. (to be published)] it was demonstrated, both experimentally and theoretically, that Auger electrons are subject to an energetic chirp if a three-body-interaction dubbed postcollision interaction (PCI) is involved. Here, we extend previous theoretical work and give a detailed analysis of field-assisted PCI based on numerical solutions of the time-dependent Schrödinger equation, extensive Monte Carlo–averaged molecular dynamics simulations, and analytical theory. The dependence on various streaking and excitation conditions is investigated, and we discuss how these findings may help to improve XUV pulse characterization as well as understanding of ultrafast atomic processes.

DOI: 10.1103/PhysRevA.85.053416 PACS number(s): 32.80.Aa, 32.80.Hd, 32.30.−r, 78.47.J−

I. INTRODUCTION

The progress in the creation of phase-stabilized laser systems and the generation of short and ultrashort pulses in the UV and XUV regimes [1,2] allows nowadays for the observation of electronic processes on the femtosecond and even sub-femtosecond time scale in a time-resolved fashion [3,4]. Fundamental investigations include the mapping of the oscillating electrical field of a laser [5], electron tunneling in strong fields [6], or the direct observation of Auger decay in the time domain [7]. Recently, processes down to a duration of several tens of attoseconds have been demonstrated to be resolvable [8].

The major tool for the observation of fast processes since early days in physics is the *streak camera*. Following its first mechanical realization by Wheatstone in 1834 [9] with μs resolution, nowadays the sub-picosecond regime can be accessed with classical optoelectronic setups [10,11]. To overcome the mechanical and electronic barriers for switching times, the answer was found in electrodynamics, leading to a setup called a light-driven streak camera [12,13]: Here, the temporal deflection of electrons is realized by the time-varying vector potential of a laser field and the triggering of the process is done by ultrashort ionization through attosecond XUV pulses in pump-probe setups. A possibility to reach the zeptosecond regime in ultrahigh fields has recently been proposed [14] theoretically.

An important application of the light-field-driven streak camera is in the characterization of (X)UV pump pulses in the femtosecond [15] and sub-fs regimes [13]. By means of photoionization of rare-gas target atoms the XUV pulse properties, such as duration, substructure, and chirp, are imprinted on a photoelectron distribution. A time-varying streaking field deflects these electrons and maps the temporal properties to a measurable energy spectrum. Therefore, this procedure strongly relies on the precise knowledge of the photon-to-electron conversion and, with that, a method to extract the temporal pulse properties from the streaked kinetic energy spectra of the electrons. While for solely photoelectrons this mapping is agreed to be understood for atoms [13,15] and atoms on surfaces [16,17], the situation strongly differs if Auger decay is involved.

The radiationless decay of resonances, first described by Meitner in 1922 [18] and Auger in 1925 [19], is a fundamental correlation-driven many-body effect in quantum mechanics, covering atoms, solids, quantum dots, and molecules. The photoexcited inner-shell hole is subject to spontaneous decay, transferring its energy to an outer-shell electron, which leaves the ion with its excess energy. The result is a doubly charged ion and two correlated electrons in the continuum. Due to the spontaneous character of the hole decay, the Auger electron cannot carry information about the pump pulse. Nevertheless, in Ref. [20] it was demonstrated, utilizing the THz streak-camera setup, that the energy of the Auger electron depends on its release time; that is, it carries an energetic chirp, if the Auger electron is faster than the preceding photoelectron. This could be verified using two independent experiments involving XUV photons from (i) the free electron laser FLASH at DESY (Hamburg) and (ii) a higher-harmonics generation (HHG) source [21]. While for (i) the ionizing pulse has a complicated structure, both in time and in energy, for (ii) chirp-free pulses with rather well-defined properties are expected. Nevertheless, it was established experimentally that for both (i) and (ii), the Auger electron's chirp is present and has qualitatively the same properties.

The authors of [20] identified postcollision interaction (PCI) as the responsible mechanism for the observed chirp, utilizing extensive molecular dynamics (MD) simulations as well as an analytically solvable model. PCI is a process where a fast Auger electron can catch up with the slower photoelectron, which leads to a drastic change of the screening of the ion's charge. This manifests itself in an energy exchange: The photoelectron loses energy (increased binding), whereas the Auger electron is correspondingly accelerated (the binding potential becomes shielded). Obviously, the net amount of transferred energy depends on the distance from the ion; the closer the overtaking happens, the stronger is the effect. Although widely discussed in the literature [22–27], the consequences of PCI for the temporal energy distribution remained unexplored. In this paper, we extend the theory presented in Ref. [20] and give a detailed description of field-assisted (FA) PCI using quantum and classical simulations as well as analytical theory.

The paper is organized as follows. In Sec. II we demonstrate the presence of a chirp on the Auger-electron energy by solving

*bauch@theo-physik.uni-kiel.de

the time-dependent Schrödinger equation (TDSE) for model systems and support the idea of PCI being the responsible mechanism. To overcome the model character necessary for quantum calculations, we develop in Sec. III a classical simulation technique based on Monte Carlo (MC) averaged MD. In Sec. IV, extending the model of [20], we present an analytical theory for the Auger line shape in the presence of a slowly varying streaking field including PCI effects and compare to TDSE as well as MC MD simulations. In Sec. V, we investigate the influence of various pulse parameters and show how the measurement of the PCI-induced chirp may help to improve the pulse characterization capabilities of light-field-driven streak-camera setups. The paper closes with a comment on recent experiments and an outlook on future investigations in Sec. VI.

II. QUANTUM THEORY OF LASER-ASSISTED AUGER DECAY

The starting point for the description of laser-assisted Auger decay (LAAD) on a quantum mechanical level is the TDSE. However, full quantum calculations of autoionization involve two or more electrons, which limit them to model studies or helium on very short time scales (see, e.g., [28,29]). To overcome this "brute-force" approach we use a generalization of Fano's theory [30] to the time-dependent case developed in Refs. [31–33] and references therein. The notations follow [33]; an analogous derivation based on quantum field theory can be found in Ref. [34]. A similar theoretical approach to time-resolved Fano resonances is developed in Refs. [35,36].

The time evolution of the outgoing photoelectron after excitation with an XUV pulse is governed by a set of coupled TDSEs (throughout atomic units, $m_e = |e| = \hbar = 4\pi\epsilon_0 \equiv 1$, are used):

$$i\frac{\partial}{\partial t}\phi_d(\boldsymbol{r},t) = \left(\hat{H}_1(\boldsymbol{r}) - i\frac{\Gamma_A}{2} - zE_L(t)\right)\phi_d(\boldsymbol{r},t) - zE_X(t)\phi_0(\boldsymbol{r})e^{-i\epsilon_0 t}, \tag{1}$$

$$i\frac{\partial}{\partial t}\phi_\epsilon(\boldsymbol{r},t) = \left(\hat{H}_2(\boldsymbol{r}) - E_A + \frac{1}{2}[\boldsymbol{k}_A - \boldsymbol{A}_L(t)]^2 - zE_L(t)\right) \times \phi_\epsilon(\boldsymbol{r},t) + V\phi_d(\boldsymbol{r},t). \tag{2}$$

Equation (1) describes the photoelectron excited from the initial orbital ϕ_0 with energy ϵ_0 by a laser pulse $E_X(t)$. It moves in a potential of a singly charged ion, included in $\hat{H}_1(\boldsymbol{r})$, and the streaking field $E_L(t)$. In other words, $\phi_d(t)$ describes the photoelectron before decay of the resonance with decay constant Γ_A. After Auger decay with excess energy E_A, being the energy difference between the outer shell electron and the core hole, the photoelectron's movement in the potential of a doubly charged ion, contained in $\hat{H}_2$, is governed by Eq. (2) coupled to Eq. (1) via the Auger decay matrix element V, which is assumed to be constant in energy and space [33]. By setting $\hat{H}_1 = \hat{H}_2$, postcollision effects due to changed screening of the ion's charge can be artificially excluded from the calculations.

In fact, Eq. (2) represents a set of equations for all possible energies of the Auger electron $\epsilon = \boldsymbol{k}_A^2/2$. The vector potential $\boldsymbol{A}_L(t)$ associated with the electrical field $\boldsymbol{E}_L(t)$,

$$\boldsymbol{A}_L(t) = -\int_{-\infty}^{t} d\tau\, E_L(\tau), \tag{3}$$

is chosen to vanish for long times.

Both laser pulses are linearly polarized in the z direction with Gaussian envelopes and coupled to Eqs. (1) and (2) in dipole approximation. The streaking pulse with duration τ_L, phase shift φ_L, and frequency ω_L is centered at zero,

$$\boldsymbol{E}_L(t) = \hat{e}_z E_L^0 \exp\left(-\frac{t^2}{2\tilde{\tau}_L^2}\right)\cos\left[\omega_L t + \varphi_L\right]. \tag{4}$$

The XUV pulse is delayed by t_X with photon energy ω_X and duration τ_X,

$$\boldsymbol{E}_X(t) = \hat{e}_z E_X^0 \exp\left(-\frac{(t-t_X)^2}{2\tilde{\tau}_X^2}\right)\cos\left[\omega_X(t-t_X)\right]. \tag{5}$$

Note that throughout this paper all pulse durations are given as full width at half maximum (FWHM) and will be denoted by $\tau_{X,L} = 2\sqrt{2\ln 2}\tilde{\tau}_{X,L}$. The model [Eqs. (1) and (2)] has been successfully applied to the recapture of photoelectrons due to PCI [37,38] and to (angle-resolved) sideband structures in LAAD [39,40], which appear if the duration of the pump pulse is comparable to or longer than the period of the streaking field. In this work, we use $\tau_X \ll 1/\omega_L$ required for streak cameras.

A. Simplifications

Up to now, the above-mentioned previous works considered short pulses in the (sub-) fs regime involving infrared (IR) streaking pulses. The characterization of pump pulses longer than 20 fs, as they are produced, for example, by free electron lasers, requires deflecting fields based on THz radiation [15,20] and, therefore, requires the propagation of Eqs. (1) and (2) over a duration of several picoseconds. In order to describe the involved processes on a time-dependent quantum mechanical level drastic simplifications are needed to keep the computational costs manageable.

As a first step, we restrict our investigations to a one-dimensional (1D) version, that is, consider wave functions of the form $\phi_d(x,t)$ and $\phi_\epsilon(x,t)$, neglecting any angular momenta and distributions. This leads to the model Hamiltonians $\hat{H}_1(x)$ and $\hat{H}_2(x)$ which are chosen to account for the correct asymptotics of the binding potentials of the remaining ion,

$$\hat{H}_i(x) = -\frac{1}{2}\frac{\partial^2}{\partial x^2} + \frac{Z_i}{\sqrt{x^2+\kappa^2}}, \tag{6}$$

with $Z_1 = -1$ and $Z_2 = -2$. The Coulomb singularity appearing in 1D systems has been regularized in a standard procedure by κ (e.g., [28,41,42]), assuring a finite binding potential at the position of the ion.

Still, to keep track of the photoelectrons traveling with 25 to 80 eV in the continuum, enormous computational grids are needed. To overcome this point, we introduce a scaling procedure of all relevant temporal quantities by a factor γ, which maps the (not-manageable) physical system to a smaller-sized analog, which can be tackled by the quantum

simulations:

$$\Gamma_A^* = \gamma\Gamma_A, \quad \omega_L^* = \gamma\omega_L, \quad \tau_X^* = \frac{\tau_X}{\gamma}, \quad \tau_L^* = \frac{\tau_L}{\gamma}. \qquad (7)$$

In order to keep the relevant streaking conditions comparable, the intensity of the streaking field is chosen such that the ponderomotive potential $U_p = E_0^2/4\omega_L^2$ of the streaking field is kept constant when γ is varied. The influence of this scaling procedure is discussed in detail below.

B. Solution of Eqs. (1) and (2)

We solve the 1D analogs of Eqs. (1) and (2) employing a finite-element discrete variable representation (FE-DVR) [43,44] and an independent finite-difference based method on large spatial grids allowing for the propagation of several tens of fs without reflections at the grid edges. All considered observables have been carefully checked for convergence with respect to the numerical discretizations.

Throughout this paper, two transitions motivated by the experiment are considered, the *NOO* transition in xenon and the *MNN* transition in krypton [20]. Let us start with xenon. For that, the eigenstate of $\hat{H}_1$ ($\kappa = 0.1935$) with a ground-state energy of $E_p = -66$ eV is used for XUV excitation with a photon energy of $w_X = 91$ eV, which corresponds to a kinetic energy of $w_X + E_p = 25$ eV for the photoelectron. The Auger-electron energy is chosen to match $E_A = 34$ eV, being faster than the photoelectron wave packet and thus giving rise to PCI effects. An example of the resulting Auger-electron line shapes for a full scan of time delays t_X is shown in Fig. 1 for a streaking with 33 THz and $U_p = 98.8$ meV and a pump pulse duration of 2.83 fs, thus scaled by a factor of $\gamma = 10$ in comparison with the THz streak camera in Ref. [15]. Analogously, the atomic parameters, matching the Xe *NOO* transition, are scaled by the same factor according to Eq. (7).

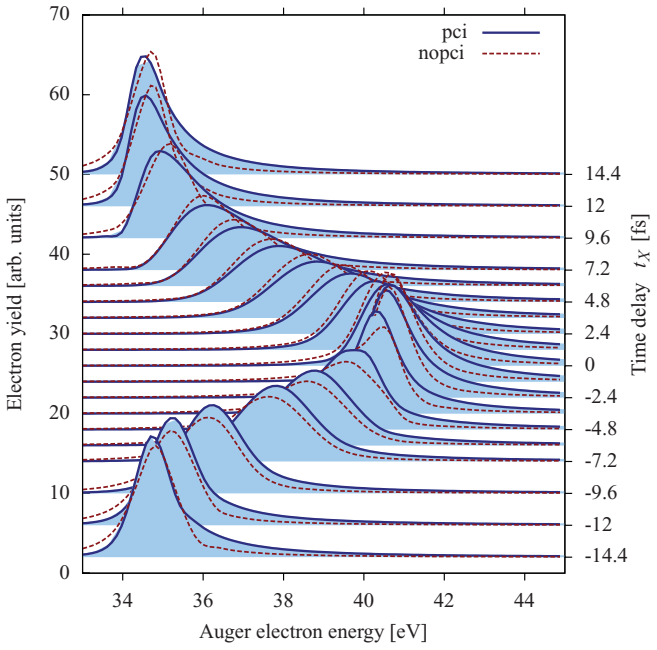

FIG. 1. (Color online) Auger line shapes obtained by solving Eqs. (1) and (2) for a series of time delays t_X. Shown is the case including PCI (blue solid lines, blue area) and the case neglecting PCI (red dashed lines), that is, $\hat{H}_2 = \hat{H}_1$ in Eqs. (1) and (2) for a 16.9-fs single-cycle ($\varphi_L = \pi/2$) streaking pulse with a frequency of $\omega_L = 33$ THz and $U_p = 98.8$ meV. The 2.83-fs XUV pulse has a photon energy of 91 eV. The Auger decay constant was set to $\Gamma_A = 950$ meV at an Auger energy of $E_A = 34.27$ eV, thus resembling THz streaking of the Xe *NOO* transition scaled by a factor of $\gamma = 10$ (see text for details). Note that the lines neglecting PCI have been shifted toward higher energy by 0.5 eV for better comparison.

Each individual Auger line is shown for two cases: including PCI (blue solid lines) and neglecting PCI (red dashed lines). For both cases, the typical streaking picture of the time-dependent momentum transfer arises, with a general shift of the PCI result toward higher energies (0.5 eV), which is compensated in Fig. 1 for better visibility. Careful inspection of the line shapes reveals that for a falling slope of $A(t)$ ($t_X < 0$) the lines are higher and of smaller width than for the case of rising slope of $A(t)$ ($t_X > 0$) (cf. pci vs nopci curves). Note that the energy shift is proportional to $-A(t)$. The lines corresponding to the case without PCI have the same height and width for positive and negative time delays.

This observation already indicates a chirp in Auger-electron emission, that is, a time-dependent variation of the energy of the Auger electron manifesting itself in an asymmetry with respect to the direction of the slope of A. In the following, this result is investigated in detail and the underlying physical mechanism is identified.

C. Analysis of the TDSE results

Let us first discuss the influence of the scaling procedure (7), shown in Fig. 2. We point out that each value of γ corresponds to a certain physical system, but our aim is to describe experiments based on the Xe *NOO* transition. The width displayed in Fig. 2 is extracted from line shape data by interpolation utilizing cubic splines and subsequent finding of the maximum and the corresponding FWHM. For better comparison, the x axis is shifted by the Auger decay time Γ_A^{-1}

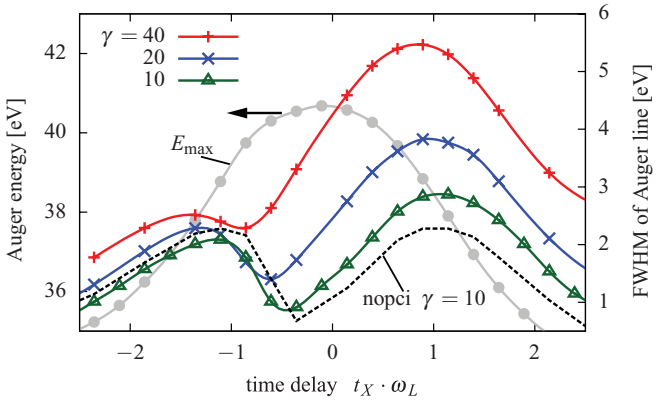

FIG. 2. (Color online) FWHM of Auger lines (right axis) obtained by solving Eqs. (1) and (2) for different scaling factors γ [cf. Eq. (7)] of the Xe *NOO* transition in a 3.3-THz streaking field keeping $U_p = 98.8$ meV constant. The natural linewidth Γ_A has been subtracted for each set of parameters for better comparison. The maximum of the line [proportional to $-A(t)$, gray line with solid circles labeled by E_{max}, left axis] and the case neglecting PCI (black dashed line) are shown for $\gamma = 10$. For $\gamma = 10$, parameters are the same as in Fig. 1.

for each data set and the width was modified by $\sqrt{\sigma^2 - \Gamma_A^2}$ to account for the different natural linewidth in each set of parameters. The first observation is a strong asymmetry in the FWHM for all values of γ with respect to the slope of $A(t)$. Note that the displayed curve labeled $E_{\max}$ shows the energy corresponding to the maximum of the Auger line, which is proportional to $-A(t)$. Approaching the physical system of Xe *NOO* ($\gamma = 1$), the asymmetry gets smaller, but is still present for the smallest considered value of γ. For comparison, also the case neglecting PCI is shown for $\gamma = 10$, where no such asymmetry is observed and the typical chirp-free streaking behavior [13] is retrieved: Largest width (and corresponding time resolution of the streak camera) occurs at maximum slope of $A(t)$. Note that for single-cycle pulses used here, this does not coincide with zero transitions of $A(t)$ (electrical field maxima). At the maximum of $|A(t)|$, as expected, a pronounced minimum can be observed.

Since the PCI effect originates from the changed screening of the remaining ions' charge during overtaking of the photoelectron by the Auger electron, it strongly depends on the velocity of the photoelectron (cf. Sec. IV C). Therefore, the observed asymmetry should be more pronounced for slow photoelectrons, where the overtaking happens in close vicinity to the ion [20], and should vanish for fast ones, where the Auger electron cannot catch up with the photoelectron. Figure 3 shows the FWHM of the Auger line of the Xe *NOO* transition ($\gamma = 10$) for a set of photon energies ω_X. As is clearly seen, the strongest asymmetry is observed for slow photoelectrons (green curve with triangles), whereas the increase of the photoelectron's energy leads to a decrease of the observed asymmetry in the FWHM and approaches the case neglecting PCI (black dashed line), thus supporting the idea that PCI is responsible for the energetic chirp in Auger emission. We note that, although for $\omega_X = 126$ eV rather fast photoelectrons (47 eV in comparison to 35 eV Auger-electron energy) are emitted (red curve), still an asymmetry is observed. This originates from a rather broad distribution of the photoelectron energy.

We can now analyze the dependence of the streaked lines upon various pulse parameters. Those with most influence on

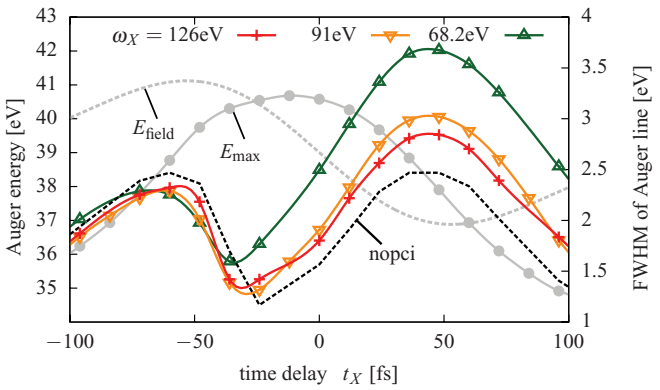

FIG. 3. (Color online) FWHM of Auger lines (right axis) for different photon energies ω_X of the XUV pulse of 28 fs duration. All other parameters are the same as in Fig. 2 for the case $\gamma = 10$. The energy of the maximum of the Auger line and the case neglecting PCI (black dashed line) are given for $\omega_X = 91$ eV. The time dependence of the electrical field $E(t)$ is sketched by the gray dotted line.

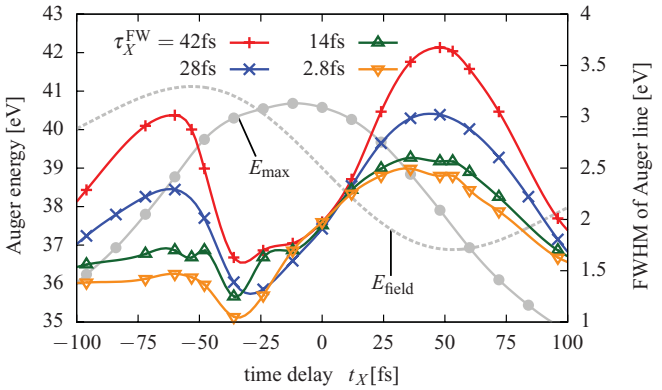

FIG. 4. (Color online) FWHM of Auger line (right axis) for different XUV pulse durations τ_X^{FW}. The maximum of the Auger line [proportional to $-A(t)$, solid circles] is shown for 28 fs. The time dependence of the electrical field $E(t)$ is sketched by the gray dotted line. Parameters are the same as in Fig. 2 for $\gamma = 10$.

the streaking mechanism are the ponderomotive potential U_p of the streaking field and the duration of the pump pulse, τ_X. In Fig. 4 the dependence of the Auger linewidth of the Xe *NOO* transition is shown for a set of XUV pulse durations for a scaling parameter of $\gamma = 10$. For larger pulse durations, a longer period of the slope of the streaking vector potential is accessible, consequently leading to a larger overall width, which is in accordance with the typical streaking mechanism. However, the asymmetry with respect to the sign of the slope of the vector potential is more pronounced for shorter pulse durations (2.8 fs). This can be attributed to the fact that for longer pulse durations the linewidth is dominated by the streaking part and for shorter pulse durations the chirp becomes dominant, which is discussed in detail in Sec. V.

For different ponderomotive potentials of the streaking field, shown in Fig. 5, a similar picture arises: The larger the ponderomotive potential, the larger is the streaking contribution leading to a relative decrease of the observed asymmetry. However, we note that for very small U_p the linewidth asymmetry must vanish because of the vanishing vector potential.

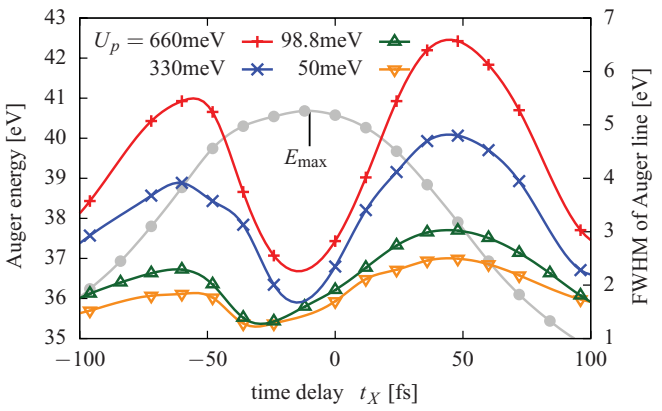

FIG. 5. (Color online) The same as Fig. 4 but for different ponderomotive potentials U_p of the streaking field at a fixed XUV pulse duration of 28 fs ($\gamma = 10$). The graph of the maximum of the line corresponds to $U_p = 98.8$ meV.

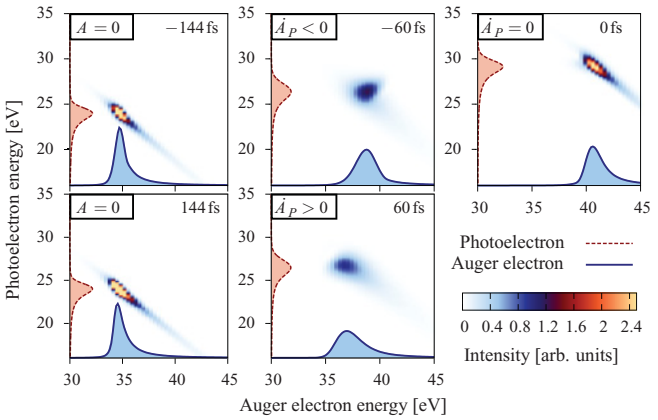

FIG. 6. (Color online) Coincidence energy spectra for Auger and photoelectrons for selected time delays t_X calculated by solving Eqs. (1) and (2). The integrated photoelectron (Auger electron) distribution is plotted with red dashed (blue solid) lines. Parameters are the same as in Fig. 1 (Xe *NOO* with $\gamma = 10$).

D. Auger-electron and photoelectron coincidence spectra

In addition to the individual kinetic energy spectra of the Auger electrons, Eqs. (1) and (2) also allow for the calculation of coincidence energy spectra of both involved electrons. This gives more detailed insight into their correlated motion. An example of the Xe *NOO* transition ($\gamma = 10$) is given in Fig. 6 for five selected time delays t_X. All spectra are dominated by a diagonal line from top left to bottom right, which indicates an energy correlation between photoelectron and Auger electron. This is due to an energy exchange between both and governed by energy conservation. For the field-free cases (±144 fs) and the maximum of the vector potential (0 fs) a rather sharp spectrum is observed, whereas at the (approximate) zero transitions of the vector potential (±60 fs) the streaking mechanism gives broad energy distributions for both the photoelectron and the Auger electron.

In addition to the integrated Auger-electron spectra (blue, solid lines), the corresponding photoelectron distribution is plotted with (red) dashed lines. A careful inspection reveals that the prominent asymmetry with respect to the slope of the vector potential (±60 fs) observed for the Auger electron is not present in the photoelectron spectra. This indicates, that the photoelectron distribution carries no energetic chirp. A more detailed description and a simple picture for this are given in Sec. IV G.

III. SEMICLASSICAL SIMULATIONS

To proceed further and compare quantitatively with current experiments, it is crucial to take into account the 3D geometry of the atom and the true time scales, that is, to avoid the scaling procedure by γ. Since this is not possible utilizing TDSE simulations, it is necessary to turn to a (semi-) classical description of FA PCI including both electrons, the ion, and the streaking field. Our classical method describing PCI is motivated by successful previous models for the field-free case [22].

The classical dynamics of both electrons is governed by Newton's equations ($m_e = 1$),

$$\begin{aligned} \ddot{\boldsymbol{r}}_P(t) &= \boldsymbol{F}_P(\boldsymbol{r}_P, \boldsymbol{r}_A, t), \\ \ddot{\boldsymbol{r}}_A(t) &= \boldsymbol{F}_A(\boldsymbol{r}_P, \boldsymbol{r}_A, t), \end{aligned} \tag{8}$$

where the photoelectron (Auger electron) is denoted by index P (A). The propagation is split into two phases: (i) before Auger decay ($t_{P_i} \leqslant t < t_{A_i}$) and (ii) after Auger decay ($t_{A_i} < t < t_d$), where t_d is the time at the detector, which determines the corresponding forces in Eq. (8).

Phase (i) [$t_{P_i} \leqslant t < t_{A_i}$]:

$$\boldsymbol{F}_P(t) = -\nabla V^+(\boldsymbol{r}_P) - \boldsymbol{E}_L(t). \tag{9}$$

Phase (ii) [$t \geqslant t_{A_i}$]:

$$\begin{aligned} \boldsymbol{F}_P(t) &= -\nabla V^{2+}(\boldsymbol{r}_P) - \boldsymbol{E}_L(t) - \nabla V_{e-e}(\boldsymbol{r}_A, \boldsymbol{r}_P), \\ \boldsymbol{F}_A(t) &= -\nabla V^{2+}(\boldsymbol{r}_A) - \boldsymbol{E}_L(t) - \nabla V_{e-e}(\boldsymbol{r}_P, \boldsymbol{r}_A). \end{aligned} \tag{10}$$

For (i) only the photoelectron is propagated in the combined field of a singly charged ion, $V^+(\boldsymbol{r})$, and the streaking field, $\boldsymbol{E}_L(t)$. In phase (ii) both electrons experience the potential of a doubly charged ion, $V^{2+}(\boldsymbol{r})$, the streaking field, and their binary interaction $V_{e-e}(\boldsymbol{r}_1, \boldsymbol{r}_2)$. All interaction potentials are of pure Coulomb type:

$$V^+(\boldsymbol{r}) = -\frac{1}{|\boldsymbol{r}|}, \quad V^{2+}(\boldsymbol{r}) = -\frac{2}{|\boldsymbol{r}|}, \tag{11}$$

$$\text{and} \quad V_{e-e}(\boldsymbol{r}_1, \boldsymbol{r}_2) = \frac{1}{|\boldsymbol{r}_1 - \boldsymbol{r}_2|}. \tag{12}$$

By setting $V_{e\text{-}e} \equiv 0$ and additionally considering $V^+ \equiv V^{2+}$, all *e-e* interactions and PCI effects can be turned off (denoted by "neglecting *e-e* interaction" in the following). The set of Eqs. (8) is completed by associated initial conditions

$$\dot{\boldsymbol{r}}_P(t_{P_i}) = \boldsymbol{p}_{P_i} \quad \text{and} \quad \boldsymbol{r}_P(t_{P_i}) = \boldsymbol{r}_{P_i}, \tag{13}$$

$$\dot{\boldsymbol{r}}_A(t_{A_i}) = \boldsymbol{p}_{A_i} \quad \text{and} \quad \boldsymbol{r}_A(t_{A_i}) = \boldsymbol{r}_{A_i}. \tag{14}$$

A. Initial condition sampling

To reproduce the quantum mechanical nature of photoionization and Auger decay in our classical model, we developed a MC sampling procedure for the initial conditions (13) and (14). During the XUV pulse, the photoelectron is released with the probability (proportional to the instantaneous intensity of the XUV pulse, $\propto E_X^2$)

$$\mathcal{P}_{T_P}(\tau_i) = \frac{1}{\sqrt{\pi}\tau_X} \exp\left(-\frac{\tau_i^2}{\tau_X^2}\right), \tag{15}$$

which creates the core hole at a time $\tau_i = t_{P_i} - t_X$. The vacancy is filled after the time $\tau_A = t_{A_i} - t_{P_i} > 0$ by lifting the Auger electron into the continuum according to the decay law (probability density; see Fig. 7 for notations)

$$\mathcal{P}_{T_A}(\tau_A) = \Gamma_A e^{-\Gamma_A \tau_A}. \tag{16}$$

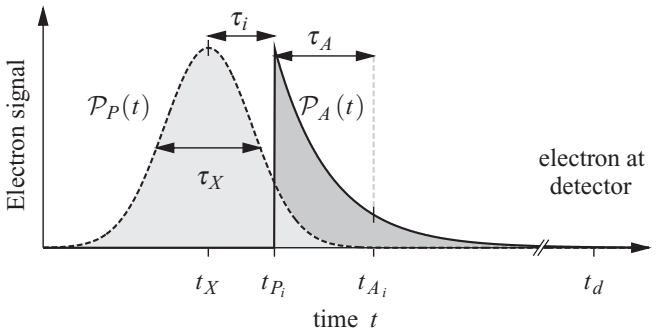

FIG. 7. Temporal parameters and electron distributions: The XUV pulse is centered at t_X with a FWHM duration of τ_X. At t_{P_i} during the pulse the photoelectron is excited, which triggers Auger decay at a time instant t_{A_i}. The measurement is performed long after the pulses and the decay are over, at time t_d ($t_d \to \infty$).

The kinetic energy distribution of the photoelectron follows a Gaussian distribution,

$$\mathcal{P}_{E_P}(E_{P_i}) = \frac{1}{\sqrt{2\pi}\sigma_X} \exp\left(-\frac{(E_{P_i} - E_{P_0})^2}{2\sigma_X^2}\right), \qquad (17)$$

with the spectral width σ_X centered around the energy $E_{P_0} = \omega_X - I_p$, with the ionization potential of the core electron I_p. The (undisturbed) line shape of the Auger electron with mean energy E_A associated with Eq. (16) is a Lorentzian distribution

$$\mathcal{P}_{E_A}(E_{A_i}) = \frac{\Gamma_A/2\pi}{(E_{A_i} - E_A)^2 + \frac{1}{4}\Gamma_A^2}. \qquad (18)$$

With that, the absolute values of the initial momenta are set by Eqs. (17) and (18) to

$$|\boldsymbol{p}_{P_i}| = \sqrt{2E_{P_i}} \quad \text{and} \quad |\boldsymbol{p}_{A_i}| = \sqrt{2E_{A_i}}. \qquad (19)$$

For small initial distances r_{P_i} and r_{A_i} of the electrons from the ion, it is important to take into account the remaining finite binding potential at the point of appearance of the electrons, $V^+(\boldsymbol{r}_{P_i})$ and $V^{2+}(\boldsymbol{r}_{A_i})$, to assure their correct asymptotic momenta on the detector. Entering as a free parameter in our model, we carefully checked the influence of different values of r_{P_i} and r_{A_i} ranging from 1 to 20 (in units of the Bohr radius) and found no significant change of the results.

The directions of $\boldsymbol{r}_{P_i}$ and $\boldsymbol{r}_{A_i}$ as well as of $\boldsymbol{p}_{P_i}$ and $\boldsymbol{p}_{A_i}$ are given by the quantum mechanical angular distributions of the associated initial state, approximated by

$$\mathcal{P}_{P \text{ or } A}(\varphi) = \frac{1}{4\pi}[1 + \beta_{P \text{ or } A}(3\cos^2\varphi - 1)], \qquad (20)$$

with the asymmetry parameter, β, being available in the literature (e.g., [45]). We note as a technical aspect, that sphere point picking [46] is crucial for the correct MC sampling of Eq. (20) to maintain the correct uniform distribution of points on a sphere.

B. Extraction of observables

We propagate Eq. (8) with initial conditions (13) and (14), randomly distributed according to Eqs. (15)–(20), utilizing a velocity Verlet algorithm with an adaptive time step size control (see, e.g., [47]). This method will be called "MC MD" simulations in the following (MD refers to the classical propagation of both interacting electrons leaving the atom).

For each run, the final momenta $\boldsymbol{p}_{P_f}$ and $\boldsymbol{p}_{A_f}$ of typically 10^6–10^7 trajectories are recorded and sorted in angle- and energy-resolved histograms until convergence is reached. The Auger-electron kinetic energy spectra are then obtained by integrating over a detector angle element of 12.5°, typical for experiments, around the field polarization axis $\hat{e}_z$. Two opposite detection directions are possible, determined by the direction of $\boldsymbol{A}$. We only show results for the detector with positive energy shift at the maximum of the single-cycle vector potential; the second detector gives the same results, but for changed sign in $\boldsymbol{A}$. In experiments it is often favorable to consider two opposing detectors to assure the same streaking conditions [20]. Postprocessing of the Auger line shapes is performed similar to the TDSE case (cf. Sec. II C). Additionally, as in the previous part, we restrict ourselves to the case of Auger electrons; the analysis of the photoelectrons can be performed in a similar way.

C. MC MD results

We may now drop the scaling procedure (7) introduced for TDSE simulations and restore the true time constants. The result for a full scan of time delays for the krypton *MNN* transition in a 1-THz streaking field with a ponderomotive potential of 80 meV is shown in Fig. 8 for the cases (i) including (blue solid lines) and (ii) neglecting (red dashed lines) *e-e*

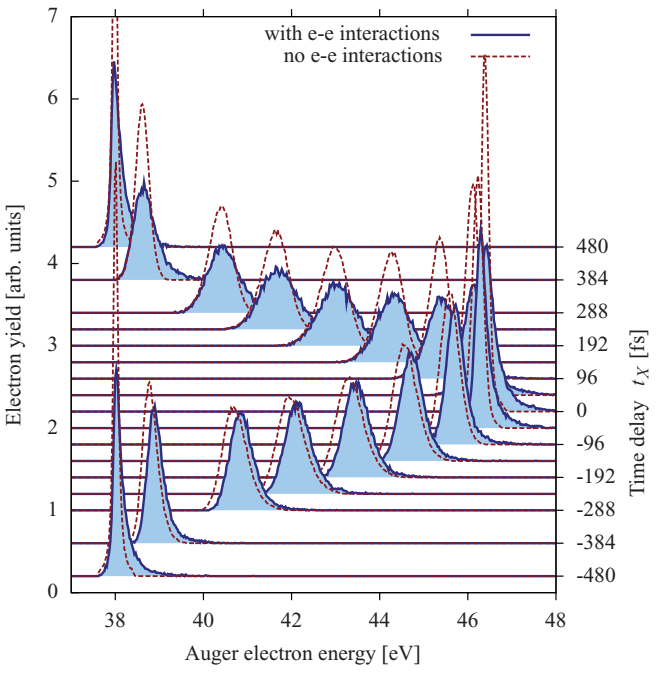

FIG. 8. (Color online) Auger line shapes of the Kr *MNN* transition for a set of time delays t_X in a 1-THz single-cycle streaking field with $U_p = 80$ meV for a XUV pulse duration of 28 fs at a photon energy of 97 eV. Results are obtained by MC averaging of MD trajectories. Shown is the case including photoelectron–Auger-electron interactions (blue solid lines) and neglecting *e-e* interactions (red dashed lines). Note that the latter lines are shifted by 100 meV toward higher energy for clarity.

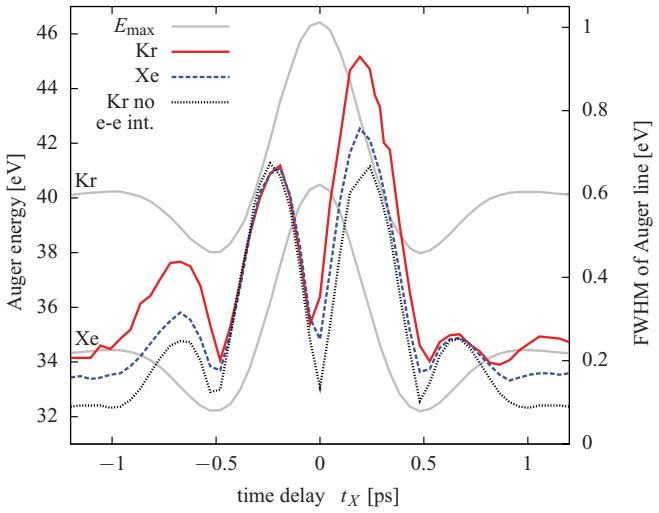

FIG. 9. (Color online) FWHM of the Auger lines (right axis) of the Xe *NOO* and Kr *MNN* transitions calculated utilizing MC MD simulations. For Xe (Kr) the photon energy of 91 eV (97 eV) leads to a photoelectron kinetic energy of 24 eV (2.6 eV). All other parameters are the same as in Fig. 8. The position of the maximum of the line, E_{max}, for both cases is shown in gray. The case neglecting *e-e* interactions for Kr is given by the black dotted line.

interactions. A similar picture as for the TDSE simulations (cf. Fig. 1) arises. A prominent asymmetry with respect to positive and negative time delays, that is, $\dot{A}(t)|_{t=t_X} \equiv \dot{A}_P > 0$ and $\dot{A}_P < 0$, respectively, can be found for (i), which completely vanishes for (ii). Note that, again, the lines with PCI effects excluded are shifted toward higher energy by 100 meV for better comparison. The shift is smaller compared to Fig. 1 due to the fact that $\gamma = 10$ overestimates PCI in the case of the TDSE simulations.

The FWHM and position of the line for the Xe *NOO* and Kr *MNN* decays are shown in Fig. 9. At the considered photon energies of 91 eV for the former and 97 eV for the latter, photoelectron energies of 24 and 2.6 eV at comparable Auger electron energies of 34 and 40 eV are observed. Due to the slow photoelectron, for Kr a dramatic increase of PCI in comparison to Xe is expected, which is connected with a stronger chirp on the Auger electron's energy. This is confirmed by our calculations (red solid lines vs blue dashed lines). If *e-e* interactions are neglected, similar line shapes and widths are observed for the rising and falling flanks of the vector potential (black dotted line). These observations are in qualitative agreement with TDSE simulations discussed in Fig. 3 and confirm that PCI is the origin for the Auger electron's chirp.

D. Comparison with TDSE

By construction, the MD simulations neglect any quantum effects in the electron dynamics, such as coherence, interference, and spin. To test the above-introduced technique, a detailed comparison of the line shapes calculated utilizing MD and TDSE methods for three different time delays is presented in Fig. 10. The Auger electron spectrum of the Xe *NOO* transition, necessarily scaled by a factor of $\gamma = 10$ for both simulations, is given for $\dot{A}_P < 0$ (left), $\dot{A}_P > 0$ (center),

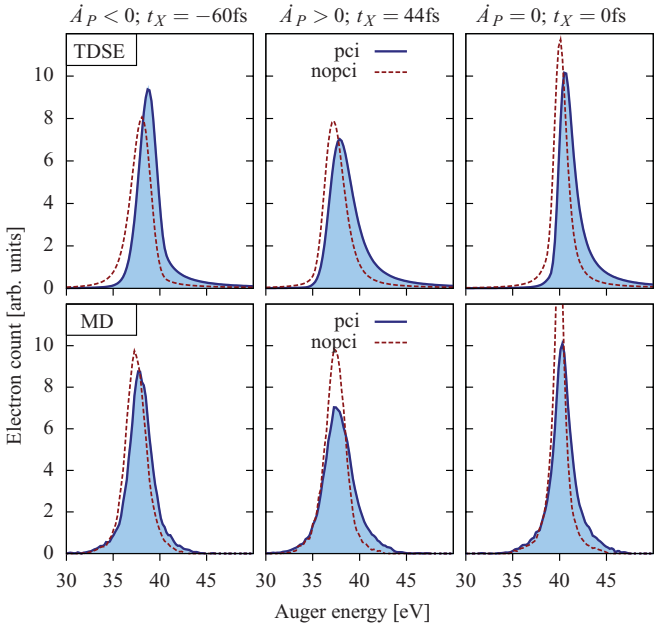

FIG. 10. (Color online) Line shapes of the Xe *NOO* transition ($\gamma = 10$) at three different time delays t_X, corresponding to the FWHM maxima (see curve in Fig. 3 for 91 eV) and $t_X = 0$, for streaking with $U_p = 98.8$ meV. Results from TDSE simulations (top row) and MC-averaged MD simulations (bottom row) are given. The cases including PCI (blue solid lines) and neglecting PCI (red dashed lines) are compared for falling (left), rising (center), and zero (right) slope of $A(t)$.

and $\dot{A}_P = 0$ (right) for situations including (solid lines) and neglecting (dashed lines) PCI. For better comparison, the Auger spectra obtained from TDSE and MD simulations have both been renormalized. This rescaling is necessary due to the small XUV ionization cross section, which has been neglected in the classical simulations.

As a first observation, the line shapes obtained by MD simulations (bottom) are slightly broadened in comparison to the TDSE (top). This can be attributed to the averaging over the finite detector acceptance angle of 12.5° in the 3D MD calculations. Here, trajectories are collected, which have been streaked with smaller amplitude due to their initial deviation (angular distribution) from the field-polarization axis. For both types of simulations, the line for $\dot{A}_P > 0$ is significantly broader than for $\dot{A}_P < 0$, which completely vanishes if PCI is turned off. Furthermore, both methods reproduce a similar PCI-induced shift of the line to higher energies. Thus, the general trends as well as the underlying mechanism for the description of the asymmetry are correctly captured by the MD model and quantum effects in the electron propagation play no dominant role for the linewidth in the considered excitation regimes.

IV. ANALYTICAL MODEL FOR AUGER LINE SHAPES

In the previous sections we have shown, utilizing TDSE and MD simulations, that Auger emission is chirped if PCI is involved, which has a prominent impact on the line shapes in external laser fields. To get deeper insight in the underlying physics, we derive closed expressions for the line shape of

the Auger electron in the streaking field including PCI effects based on a classical 1D model.

A. Time-to-energy mapping

The key mechanism of streaking is the mapping between a temporal process and the measurable energy or momentum distribution. For Auger electrons, the temporal distribution follows the decay law [Eq. (16)]. The corresponding probability to find the Auger electron in the continuum at a time t is given by

$$\mathcal{P}_A(t) = \int_0^t d\tau_A \mathcal{P}_{T_A}(\tau_A), \tag{21}$$

which approaches unity for long times (see Sec. III A and Fig. 7 for notations). The distribution (21) is translated by the streaking field to energy; thus, the quantity of interest is the kinetic energy change of the Auger electron measured at a remote detector at time t_d. Its final momentum is given by $p_{A_i} + \Delta p(t_{A_i})$. The field-induced momentum change evaluates to

$$\Delta p = -\int_{t_{A_i}}^{t_d} d\bar{t}\ E(\bar{t}) = -A\big(t_{A_i}\big), \tag{22}$$

where vanishing of the vector potential for $t = t_d$ with $t_d \to \infty$ is assumed. With that, we obtain for the Auger electron energy change

$$E^d_{\rm kin} = \frac{1}{2}\left[p_{A_i} - A\big(t_{A_i}\big)\right]^2 + \Delta E^{\rm PCI} - \frac{p_{A_i}^2}{2}. \tag{23}$$

A possible energy exchange between photoelectron and Auger electron due to PCI is accounted for by $\Delta E^{\rm PCI}(t_X, \tau_A)$. It depends on the distance from the ion, that is, on the Auger time delay τ_A, and the pump-probe time delay t_X. In the following we consider fixed (sharp) initial momenta of the two electrons, p_{P_i} and p_{A_i}.

Let us first assume an infinitesimal duration of the pump pulse ($\tau_X \to 0$), which corresponds to $t_{P_i} \equiv t_X$. An extension of the model to finite XUV pulse durations is presented in Sec. IV F. Expanding A around t_{P_i} to second order gives for the τ_A-dependent energy shift $\epsilon_S^{\rm PCI} \equiv E^d_{\rm kin} + p_{A_i} A_P$

$$\epsilon_S^{\rm PCI} \approx -p_{A_i}\left(\dot{A}_P \tau_A + \tfrac{1}{2}\ddot{A}_P \tau_A^2\right) + \Delta E^{\rm PCI}(\tau_A). \tag{24}$$

Here we use the notations $A_P \equiv A(t_{P_i})$, $\dot{A}_P = \partial/\partial t A(t)|_{t=t_{P_i}}$, and $\ddot{A}_P = \partial^2/\partial t^2 A(t)|_{t=t_{P_i}}$ and neglect higher-order terms $O(\tau_A^3\omega_L^3, A^2)$. Equation (24) translates the temporal distribution of Auger electrons governed by Eq. (21) to the energy domain through action of the streaking vector potential and PCI. This procedure was first applied in Ref. [23] for the time-to-energy transformation due to PCI without external fields. In the present paper, we demonstrate, extending the simplified model of Ref. [20], this mapping including PCI and streaking, which gives direct access to closed expressions for the Auger line shape of FA PCI.

B. Line shapes neglecting PCI

Let us first consider the case $\Delta E^{\rm PCI} = 0$ in Eq. (24) and find the Auger line shapes at characteristic pump-probe time delays t_X for zero transitions and maxima of $A(t)$.

1. Zero transitions of the vector potential

Since $\dot{A}_P \neq 0$, the leading contribution to the mapping (24) is linear in τ_A and higher-order contributions can be dropped, which gives

$$\tau_A = -\frac{\epsilon}{p_{A_i}\dot{A}_P}. \tag{25}$$

Substituting expression (25) in Eq. (21) gives the Auger line shapes for increasing (+) and decreasing (−) slope of A,

$$f_{1\pm}(\epsilon) = \Gamma_1 e^{\pm\Gamma_1\epsilon}, \quad \text{with} \quad \Gamma_1 = \frac{\Gamma_A}{p_{A_i}|\dot{A}_i|}, \tag{26}$$

with the normalization conditions

$$\int_{-\infty}^{0} d\epsilon\ f_{1+}(\epsilon) = 1, \quad \text{and} \quad \int_0^{\infty} d\epsilon\ f_{1-}(\epsilon) = 1. \tag{27}$$

The comparison with 1D MD simulations for $\tau_X \to 0$, neglecting PCI and without sampling of the initial momentum p_{A_i}, is shown in Fig. 11 for Xe *NOO* decay in a 1-THz streaking field. The streaked lines exhibit the same exponential decay law as the time dependence of the core hole decay. The direction of the slope of A only affects the orientation of the exponential tail. Deviations of Eq. (26) from the numerical solution are very small and are due to the linearization of A and are only visible in the logarithmic representation (insets in Fig. 11).

2. Extrema of the vector potential

For maxima ($\ddot{A}_P < 0$) and minima ($\ddot{A}_P > 0$) of the vector potential, $\dot{A}_P = 0$ holds; thus, the second order in τ_A is the leading contribution in Eq. (24). Because obviously $\tau_A \geqslant 0$,

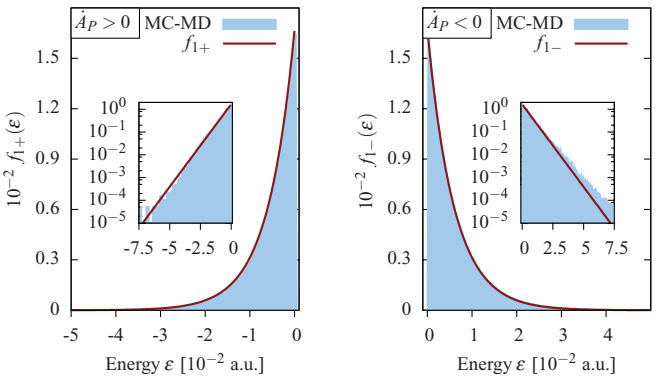

FIG. 11. (Color online) Analytical model for the Auger line shape neglecting PCI [Eq. (26)] compared to corresponding MD simulations (excluding PCI and sampling of p_{A_i}) at zero transitions of the vector potential for increasing (left) and decreasing (right) slope of A. Shown is Xe *NOO* in a 1-THz streaking field with a duration of 1 ps and a ponderomotive potential of 100 meV. The insets show the same data semilogarithmically.

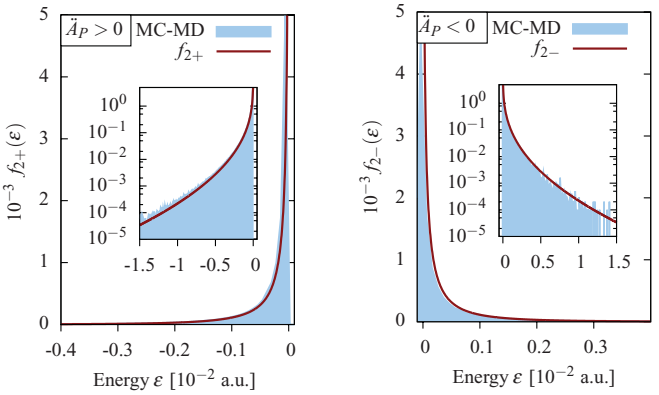

FIG. 12. (Color online) Auger line shape for minima (left panel, $\ddot{A}_P > 0$) and maxima (right panel, $\ddot{A}_P < 0$) of A. Displayed is Eq. (29) compared to MD simulations. Parameters are the same as for Fig. 11.

we obtain only one solution:

$$\tau_A = \sqrt{-\frac{2\epsilon}{\ddot{A}_P p_A}}. \tag{28}$$

The corresponding line shapes for maxima ("−") and minima ("+") of A evaluate to

$$f_{2\pm}(\epsilon) = \frac{\Gamma_2}{2}\frac{1}{\sqrt{|\epsilon|}} e^{-\Gamma_2\sqrt{|\epsilon|}}, \quad \Gamma_2 = \Gamma_A\sqrt{\frac{2}{p_{A_i|\ddot{A}_P|}}}, \tag{29}$$

with the normalizations

$$\int_{-\infty}^{0} d\epsilon\ f_{2+}(\epsilon) = 1, \quad \text{and} \quad \int_{0}^{\infty} d\epsilon\ f_{2-}(\epsilon) = 1. \tag{30}$$

The comparison with MD data is given in Fig. 12. The line is dominated by a sharp onset at zero and a rather rapid decay. The second-order expansion of A gives perfect agreement with the simulation (logarithmic representation given in the insets in Fig. 12).

C. Analytical model for PCI

We now consider the case $\Delta E^{\mathrm{PCI}} \neq 0$ in Eq. (24). To obtain closed expressions for the line shapes including streaking and PCI, the (semi-)classical model introduced in Sec. III needs to be simplified in order to calculate ΔE^{PCI}. Following [23,24], we neglect the direct electron-electron interaction and model the PCI energy exchange by an instantaneous change in the ionic binding potential of X^{2+} to X^{+} for the Auger electron and X^{+} to X^{2+} for the photoelectron. The propagation scheme, sketched in Fig. 13, then reads as follows.

Phase 1 ($t < t^*$), propagation of the photoelectron ($t > t_{P_i}$) and the Auger electron ($t > t_{A_i}$) without interaction in the streaking field $E_L(t)$:

$$\ddot{r}_P = -E_L(t) \quad \text{and} \quad \ddot{r}_A = -E_L(t), \tag{31}$$

with initial conditions

$$\begin{aligned} r_P(t_{P_i}) &= r_{P_i}, \quad p_P(t_{P_i}) = p_{P_i}, \\ r_A(t_{A_i}) &= r_{A_i}, \quad p_A(t_{A_i}) = p_{A_i}. \end{aligned} \tag{32}$$

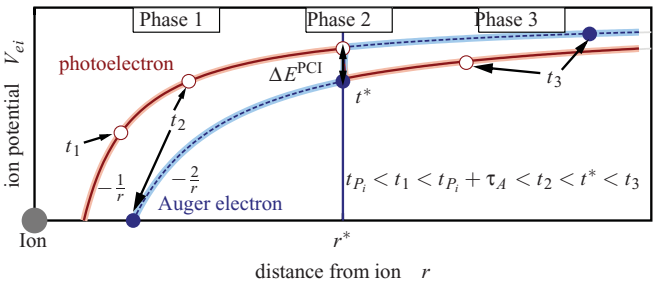

FIG. 13. (Color online) Scheme of simplified 1D propagation with PCI effects: In phase 1 ($t < t^*$), the Auger electron (solid circles) catches up with the slow photoelectron (open circles) and overtakes it at $t = t^*$ (phase 2); $p_A > p_P$ is assumed. The propagation toward the detector in phase 3 ($t > t^*$) is similar to phase 1. Figure after Ref. [20].

Phase 2 ($t = t^*$), the Auger electron overtakes the photoelectron, changed screening of the ion's charge leads to energy exchange $\pm\Delta E^{\mathrm{PCI}} = 1/r^*$ corresponding to a momentum change of

$$\begin{aligned} p_P \to p_P^- &= p_P + \Delta p_P(\Delta E^{\mathrm{PCI}}, t^*), \\ p_A \to p_A^+ &= p_A + \Delta p_A(\Delta E^{\mathrm{PCI}}, t^*). \end{aligned} \tag{33}$$

Phase 3 ($t > t^*$), similar to phase 1 but with initial conditions

$$\begin{aligned} &r_P(t^*) = r_A(t^*) = r^*; \\ &p_P(t^*) = p_P^- \quad \text{and} \quad p_A(t^*) = p_A^+. \end{aligned} \tag{34}$$

A straightforward integration of Eq. (31) gives the time of overtaking,

$$t^* = t_{A_i} + \frac{\tau_A \tilde{p}_P - r_{AP}}{p_{AP}}, \tag{35}$$

and the corresponding distance from the ion

$$r^* = \tau_A p_r + \delta r^*. \tag{36}$$

Here, we introduced the notations

$$\begin{aligned} \tilde{p}_P &\equiv p_{P_i} - A(t_{P_i}), \\ \tilde{p}_A &\equiv p_{A_i} - A(t_{A_i}), \end{aligned}$$

and

$$r_{AP} \equiv r_{A_i} - r_{P_i} - \int_{t_{P_i}}^{t_{A_i}} d\tilde{t} A(\tilde{t}),$$

$$p_{AP} \equiv \tilde{p}_A - \tilde{p}_P = p_{A_i} - p_{P_i} + A(t_{P_i}) - A(t_{A_i}),$$

$$p_r \equiv \frac{p_{A_i} p_{P_i}}{p_{AP}},$$

$$\delta r^* \approx \frac{\tilde{p}_A r_{P_i} - \tilde{p}_P r_{A_i} - A(t_{A_i})(r_{A_i} - r_{P_i})}{p_{AP}}.$$

With that, we obtain from Eq. (24) the τ_A dependence of the time-to-energy mapping function including PCI and streaking:

$$\epsilon^{\mathrm{PCI}}(\tau_A) = -p_{A_i}\dot{A}_p \tau_A + \frac{1}{p_r \tau_A + \delta r^*}. \tag{37}$$

The distance δr^* depends on the initial coordinates of the two electrons and their field-changed initial momenta. In

most cases δr^* will be a small correction to r^*. However, for situations with slow photoelectrons and relatively fast Auger electrons, that is, situations with strong PCI, δr^* may become large. In the following, we derive generalized Auger line shapes for FA PCI, improving the results presented in Ref. [20], where $\delta r^* = 0$ was assumed.

D. FA PCI without streaking

Before using the full mapping, let us neglect the first term in Eq. (37) linear in τ_A that is attributed to the streaking contribution discussed before. Then we have a hyperbolic mapping function,

$$\epsilon_0^{\mathrm{PCI}} = \frac{1}{p_r \tau_A + \delta r^*}. \tag{38}$$

Utilizing Eq. (38), the straightforward transformation of the time distribution (21) gives for the PCI-induced energy change of the Auger line shape

$$f_{3\pm}(\epsilon) = \Gamma_3 \frac{1}{\epsilon^2} e^{\Gamma_3(\delta r^* - 1/\epsilon)}, \quad \text{with} \quad \Gamma_3 = \frac{\Gamma_A}{p_r}, \tag{39}$$

$$\int_0^{1/\delta r^*} d\epsilon \; f_3(\epsilon) = 1, \tag{40}$$

where "+" ("−") refers to $\dot{A}_P > 0$ ($\dot{A}_P < 0$) in p_r and δr^*. From Eq. (39) we can immediately read off the energy distribution for the field-free case (and assuming $\delta r^* = 0$),

$$f_3^{(0)}(\epsilon) = \frac{\Gamma_A}{p_r^0} \frac{1}{\epsilon^2} e^{-\Gamma_A/(p_r^0 \epsilon)}, \tag{41}$$

with $p_r^0 = p_{P_i} p_{A_i}/(p_{P_i} - p_{A_i})$, in accordance with the result given in Ref. [23]. Our result (39) differs in the way that, although we exclude the explicit streaking contribution in Eq. (37), the field-changed initial momenta $\tilde{p}_P$ and $\tilde{p}_A$ are included. An example of Xe *NOO* in a 1-THz streaking field is shown in Fig. 14. In addition to the case of positive and negative slope of A, the field-free case [Eq. (41)] is displayed. For this specific case, no strong influence of the field on the pure PCI process is visible. However, f_{3+} has a slightly higher maximum, corresponding to smaller width, in contrast to the effect observed in the simulations in the previous section (note that this asymmetry is not the observed chirp). $f_3^{(0)}$ is exactly in the middle between both.

E. Auger line shapes including FA PCI

Using the full mapping function (37) gives a quadratic equation for τ_A,

$$\tau_A^2 + \tau_A \left(\frac{p_r \epsilon^{\mathrm{PCI}} + \delta r^* p_{A_i} \dot{A}_P}{p_r p_{A_i} \dot{A}_P} \right) + \frac{\delta r^* \epsilon^{\mathrm{PCI}} - 1}{p_r p_{A_i} \dot{A}_P} = 0. \tag{42}$$

For the inversion of Eq. (37), we assume $p_r(\tau_A) \equiv p_r$; hence, we neglect the additional implicit τ_A dependence, which enters through the vector potential. We define

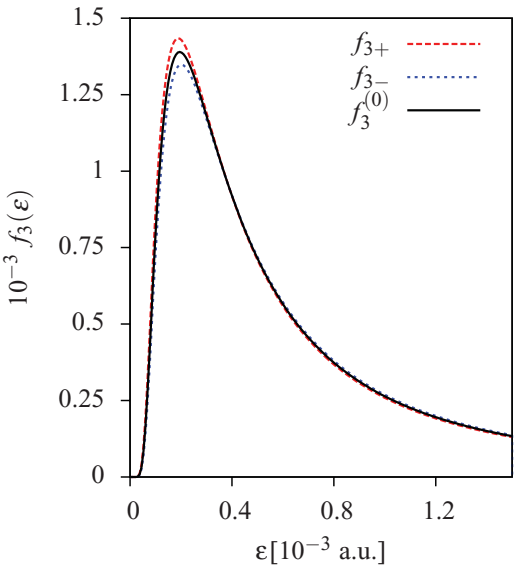

FIG. 14. (Color online) Field-assisted PCI without streaking contribution at zero transitions of A. Shown is Eq. (39) for $\dot{A} > 0$ (red dashed line) and $\dot{A} < 0$ (blue dotted line) in comparison to the field-free case [Eq. (41)]. Data is for *NOO* transition of Xe in a 1-THz streaking field with $U_p = 100$ meV for $\delta r^* = 1$.

$$\epsilon_\pm \equiv \epsilon \pm \frac{\beta}{4} \delta r^*; \quad \alpha \equiv \frac{1}{2 p_{A_i} \dot{A}_P}; \quad \beta \equiv \frac{4 p_{A_i} \dot{A}_P}{p_r} \tag{43}$$

and obtain

$$\tau_{A\pm} = -\alpha \epsilon_+ \pm \alpha k_+, \tag{44}$$

with $k_\pm = \sqrt{\epsilon_-^2 \pm |\beta|}$. For $\dot{A}_P > 0$, only the positive branch τ_{A+} can be realized ($\tau_A \geqslant 0$), which gives for the line shape with $\Gamma_4 = |\alpha| \Gamma_A$:

$$f_+(\epsilon) = \Gamma_4 \frac{k_+ - \epsilon_-}{k_+} e^{-\Gamma_4 (k_+ - \epsilon_+)}. \tag{45}$$

For $\dot{A}_P < 0$, both solutions (44), τ_{A+} and τ_{A-}, are possible. Thus, the temporal distribution function (21) is split into two parts, $\int_0^{\tau_{\min}} e^{-\Gamma_A \tau_A} d\tau_A + \int_{\tau_{\min}}^{\infty} e^{-\Gamma_A \tau_A} d\tau_A$, where $\tau_{\min}$ separates both branches, τ_{A+} and τ_{A-}, at $\epsilon(\tau_{\min}) = \epsilon_0$. The straightforward transformation of both integrals to energy gives for the joint energy distribution function

$$f_-(\epsilon) = 2\Gamma_4 e^{-\Gamma_4 \epsilon_+} \left(\frac{\epsilon_-}{k_-} \cosh \Gamma_4 k_- - \sinh \Gamma_4 k_- \right). \tag{46}$$

The line shapes of Xe *NOO* for both cases, $\dot{A}_P > 0$ and $\dot{A}_P < 0$, are given in Fig. 15 for $\delta r^* = 1$. While for the former the line is broadened by PCI, for the latter the line is compressed and completely different line shapes for subsequent zero transitions of A with different sign of the slope are observed. As in the previous cases, perfect agreement with simulations based on numerical solutions of Eqs. (31)–(34) by means of MC-averaged MD simulations (in analogy to Sec. III, but without momentum averaging) is observed, and the linearization of A has, in the considered regimes of pulse duration and ponderomotive potential, no significant influence on the streaked Auger spectra.

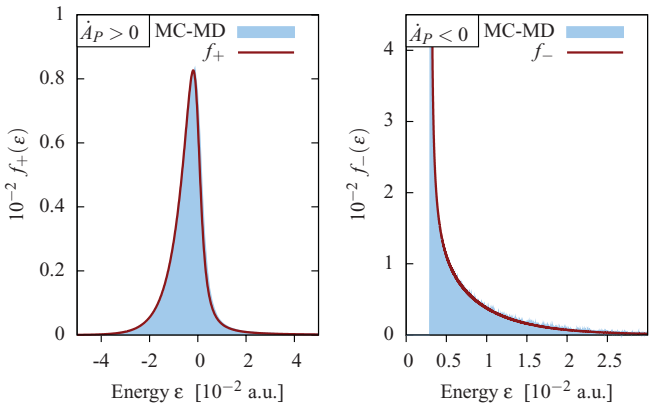

FIG. 15. (Color online) Auger line shapes at zero transition of A including streaking and PCI contributions. The analytical line shapes [Eqs. (45) and (46)] (bold, red lines) are compared to MD simulations (filled area). The case of $\dot{A}_P > 0$ ($\dot{A}_P < 0$) is shown in the left (right) panel. Parameters are the same as for Fig. 14.

To explain the strikingly different shape of the Auger lines in Fig. 15, the mapping functions from time to energy are shown in Fig. 16 for the same set of parameters. The linear streaking part contributing to Eq. (37) is plotted with blue dashed lines, the hyperbolic PCI term with green dotted lines, and the sum of both results in the red solid lines. By comparing $\dot{A}_P > 0$ (left) and $\dot{A}_P < 0$ (right), the cause for the different line shapes becomes visible: Whereas for the former, both terms add up to a bijective mapping function spanning the whole energy axis from $-\infty$ to ∞, for the latter one a forbidden energy region for $\epsilon < \epsilon_0 = 2\sqrt{p_A|\dot{A}_P|/p_r}$ occurs (gray line in Fig. 16). This leads to a drastic compression of the line (right panel in Fig. 15), where Auger electrons released at two different time moments can be mapped into the same energy interval. This situation is completely absent for

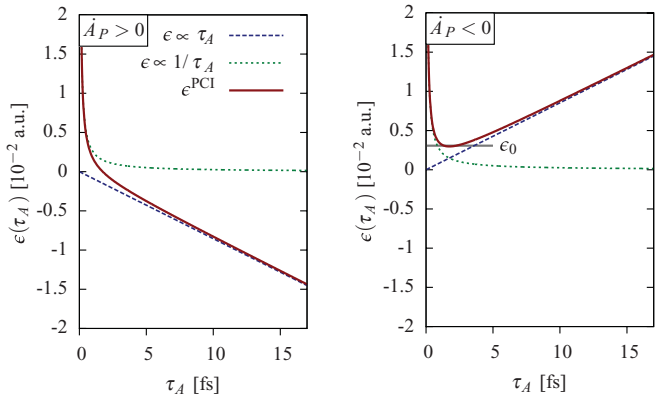

FIG. 16. (Color online) Time-to-energy mapping of the Auger electrons in the streaking field for $\dot{A}_P > 0$ (left) and $\dot{A}_P < 0$ (right). The mappings without PCI [Eq. (25), blue dashed lines], without streaking [Eq. (38), green dotted lines], and including PCI and streaking [Eq. (37) red solid lines] are shown. Different signs of $\dot{A}_P$ lead to a drastic change of the mapping: For $\dot{A}_P > 0$ the whole energy space is accessible in a bijective way, whereas in contrast for $\dot{A}_P < 0$ a forbidden region below ϵ_0 occurs and "early" and "late" Auger electrons are mapped to the same energy.

$\dot{A}_P > 0$, which leads to a broad distribution of Auger electrons (cf. left panel in Fig. 15). This effect is a direct consequence of the interplay between the hyperbolic PCI-induced chirp on the Auger electron energy, $\Delta E^{\rm PCI} \propto 1/r^* \propto 1/\tau_A$, and the linear "chirp" introduced by the streaking field, where the sign of the latter depends on the direction of the streaking field at the time of the core hole creation. An experimental verification of this mechanism utilizing XUV pulses from FLASH and HHG exciting the Xe *NOO* and Kr *MNN* transitions has been presented in Ref. [20]. The comparison of the experimentally obtained Auger electron spectra with the theoretical results calculated based on MC MD simulations, as presented in Sec. III, shows perfect agreement.

F. Finite XUV pulse duration

Equations (45) and (46) describe the shape of the Auger energy distribution for infinitesimal pulse duration of the XUV excitation. To account for finite pulse durations τ_X, a similar transformation of probability distributions from time to energy as for the case of the decay law (21) needs to be performed. The temporal distribution of a photoelectron excited by a Gaussian shaped pulse is described by Eq. (15). At zero transitions of the vector potential, utilizing the same linearization of A as was used for Eq. (24), we obtain for the τ_i-dependent energy shift (see Fig. 7 for notations),

$$\tilde{\epsilon}(\tau_i) = -p_{A_i}\dot{A}(t_X)\tau_i + O\left(A^2, \tau_i^2\right). \tag{47}$$

Using this mapping function, a streaked energy spectrum due to the finite XUV pulse duration can be calculated:

$$f_X(\tilde{\epsilon}) = \frac{1}{\sqrt{\pi}\Gamma_{X1}} \exp\left(-\frac{\tilde{\epsilon}^2}{\Gamma_{X1}^2}\right), \tag{48}$$

with the normalization condition

$$\int_{-\infty}^{\infty} d\tilde{\epsilon}\; f_X(\tilde{\epsilon}) = 1, \quad \text{and} \quad \Gamma_{X1} = p_{A_i}\dot{A}(t_X)\tau_X. \tag{49}$$

At each photoelectron "birth" time t_{P_i}, the Auger "clock" starts, and with that the energy mapping of the temporal distribution of Auger electrons. Therefore, the final streaked Auger energy distribution is given by the convolution

$$f_{XA}(\epsilon) = \int_{-\infty}^{\infty} d\tilde{\epsilon}\; f_X(\tilde{\epsilon}) f_A(\epsilon - \tilde{\epsilon}). \tag{50}$$

If the PCI contribution is neglected, that is, $f_A(\epsilon) = f_{1\pm}(\epsilon)$ [cf. Eq. (26)], the integration in Eq. (50) can be carried out analytically and gives for the line shape

$$f_{X1\pm}(\epsilon) = \frac{\Gamma_1}{2} e^{\frac{1}{4}\Gamma_{X1}^2\Gamma_1^2} e^{\pm\Gamma_1\epsilon} \operatorname{erfc}\left(\frac{\Gamma_{X1}\Gamma_1}{2} \pm \frac{\epsilon}{\Gamma_{X1}}\right). \tag{51}$$

The line shape for two subsequent zero transitions of A for an XUV pulse duration of 20 fs FWHM is shown in Fig. 17 (bold red line). The finite excitation time interval of the core hole broadens the pure Auger decay line (blue dashed line). Despite the rather long pulse duration compared to the core hole lifetime, the exponential decay of the case of infinitesimal excitation duration is still imprinted on the convoluted line. Corresponding MD data [blue area, according to method (i) below] is in perfect agreement with Eq. (51).

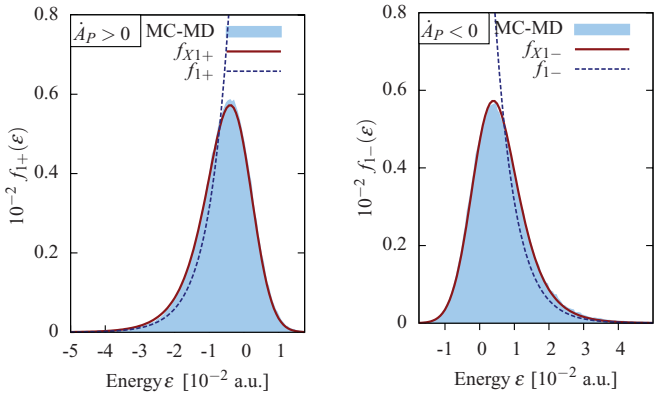

FIG. 17. (Color online) Auger line shapes for zero transitions of A neglecting PCI contributions for a finite XUV pulse duration of 20 fs FWHM. All parameters refer to THz streaking of the Xe *NOO* transition. The convoluted line shape [Eq. (51)] (bold red line) is plotted against MD simulations (blue area). The case of infinitesimal XUV pulse duration [Eq. (26)] is shown also for comparison (blue dashed lines).

Considering the PCI-distorted line shapes, $f_A(\epsilon) = f_\pm(\epsilon)$, the integral

$$f_{X\pm}(\epsilon) = \int_{-\infty}^{\infty} d\tilde{\epsilon}\; f_X(\tilde{\epsilon}) f_\pm(\epsilon - \tilde{\epsilon}) \tag{52}$$

cannot be solved analytically. The result of a numerical integration of Eq. (52) for a 20-fs FWHM XUV pulse is given in Fig. 18 for positive and negative slope of $A(t)$. Although the asymmetry with respect to $\dot{A}_P > 0$ and $\dot{A}_P < 0$ is less pronounced than for the case of infinitesimal XUV excitation duration shown in Fig. 15, still a difference between ascending and descending slope of A is visible, indicating the chirp in Auger emission. To verify the accuracy of the analytical result, additionally three different sets of simulations are shown: (i) numerical solutions according to Eqs. (31)–(34) [(blue) solid area], (ii) similar to (i) but with proper averaging over the initial momenta p_{A_i} and p_{p_i} [blue dashed lines], and (iii) 3D MD simulations according to the scheme in Sec. III, also including angular distributions [orange dotted lines]. Set (i) resembles the assumptions of the analytical model, except for the linearization of A, and shows perfect agreement with Eq. (52). Solutions according to (ii) and (iii) show a substantial broadening of the Auger line. For (ii) this results from the natural Auger linewidth and the bandwidth of the XUV pulse, and for (iii) in addition from the angle integration. This broadening occurs in a similar way for the rising and falling flanks of A and does not affect the observed asymmetry attributed to the PCI-induced chirp. Therefore, the analytical line shape model (52) catches the important features of FA PCI. It can be evaluated numerically for a large set of parameters due to its simple convolution structure. Thus, Eq. (52) is well suited for the detailed investigation of the properties of FA PCI and its dependence on the streaking conditions and XUV parameters.

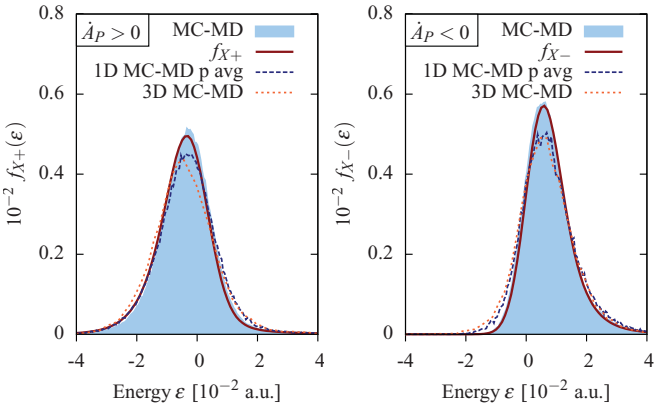

FIG. 18. (Color online) The same as Fig. 17 but for the case including PCI. The result of a numerical convolution [Eq. (52)] (red bold lines) is compared to MD simulations with sharp momenta (blue area) and with proper sampling over initial momenta p_{P_i} and p_{A_i} (blue dashed lines). Additionally, 3D MD simulations (cf. Sec. III) are shown (orange dotted lines).

G. Photoelectron distributions

In the previous sections, we identified the physical mechanism for the observed time-dependent chirp on the Auger electron's energy: a direct connection between the time instant of decay and an associated (unique) energy shift mediated through PCI. At this point, a remark on the consequences for the corresponding photoelectron distribution is appropriate. As a matter of fact, the kinetic energy of the photoelectron is affected in a similar way as it is for the Auger electron, but, by reason of energy conservation, with an opposite sign. Thus, the photoelectron is slowed down due to PCI by the same amount of energy ΔE^{PCI} the Auger electron has gained.

However, this does not result, as one might guess, in a chirp on the photoelectron energy distribution with different sign, as already pointed out in Sec. II D. The results of TDSE simulations, carried out as described in Sec. II, are shown in Fig. 19. The FWHM for the photoelectron line is depicted for the case including PCI (solid line) and neglecting PCI (dashed line) for a full set of time delays between pump and probe pulse. For both cases, no asymmetry with respect to the rising and the falling flanks of the vector potential is observed. Only

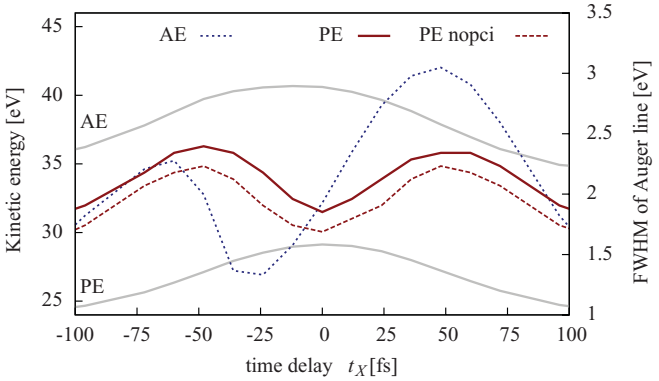

FIG. 19. (Color online) Energy (left axis) and FWHM (right axis) of the Auger electron (dotted) and the photoelectron distribution (PCI, solid; without PCI, dashed). Shown is the case of Xe *NOO* scaled by $\gamma = 10$ obtained within TDSE simulations. Parameters are the same as for Fig. 4.

a broadening of the line for the PCI-included case is present, resulting in an equidistant upward shift of the PCI curve in comparison to the case neglecting PCI, and therefore, no chirp on the photoelectron energy can be identified. The prominent asymmetry in the FWHM for the Auger electron is shown for comparison with dotted lines in Fig. 19.

Returning to Eq. (37), the mapping from the time moment of Auger decay, τ_A, to energy, the origin for the absence of a chirp becomes clear: While for Auger electrons, each decay time corresponds to a certain amount of energy transfer, for photoelectrons no such connection can be found. For each time moment of photoemission, every Auger decay time τ_A is possible, and with that any arbitrary energy transfer due to PCI. Thus, only a PCI broadening of the line is expected, which is the same for every release time of the photoelectron and explains the observed delay dependence of the FWHM of the photoelectron spectrum in Fig. 19.

V. USE OF FA PCI FOR PULSE CHARACTERIZATION

In this last part we ask whether the PCI-induced asymmetry with respect to the direction of the slope of the vector potential may help to improve the pulse characterization capabilities of the streak camera. In Sec. II we commented on the influence of the ponderomotive potential and the XUV pump pulse duration on the observed asymmetry. This raises the question of whether this dependence, especially on the pulse duration τ_X, can be used as a sensitive parameter to recover the pulse durations in experiments. Due to the larger effect of PCI, we choose Kr *MNN* decay at a photon energy of 97 eV in the following.

The line shape for different XUV pulse durations at the zero transitions of the vector potential with $U_p = 100$ meV is shown in Fig. 20, calculated according to Eq. (52). The left panel shows the broadened line f_X^+ for $\dot{A} > 0$ and the right panel the corresponding compressed line f_X^- for $\dot{A} < 0$. For the shortest pulse durations (3.5 and 7 fs) with $\tau_X \lesssim \Gamma_A^{-1}$ the largest asymmetry is observed, whereas for long pulses (42 fs) no clear distinction between $\dot{A} > 0$ and $\dot{A} < 0$ is possible. The largest impact on this asymmetry has the compressed line, which is sharp in the case of very short

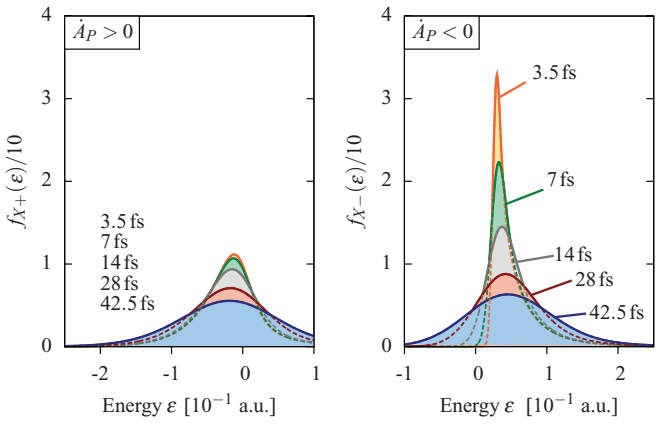

FIG. 20. (Color online) Auger line shape of the Kr *MNN* transition in a 3.3-THz streaking field at fixed ponderomotive potential of 100 meV for different XUV pulse durations with a photon energy of 97 eV. Shown are solutions of the analytical model [Eq. (52)].

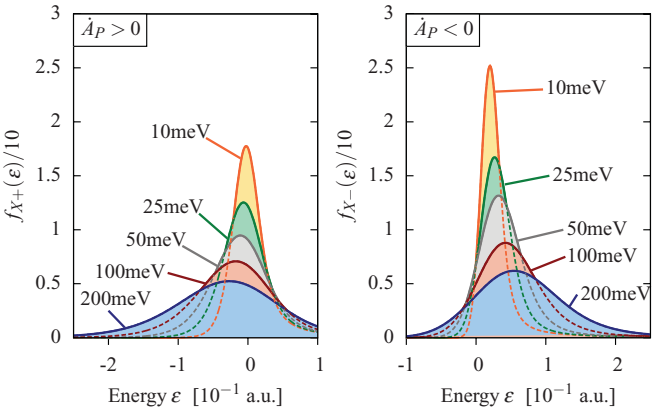

FIG. 21. (Color online) The same as Fig. 20 but for different ponderomotive potential of the streaking field at fixed XUV pulse duration of 28 fs.

pump pulses (cf. Fig. 15, right panel). For increasing τ_X, the convolution with the Gaussian-shaped time distribution of the XUV excitation smoothens (broadens) this line, until the streaking-induced broadening predominates. This result agrees qualitatively with the TDSE simulations presented above in Sec. II C (cf. Fig. 4).

A similar behavior is observed upon change of the ponderomotive potential of the streaking pulse at a fixed pump pulse duration of 28 fs, see Fig. 21. Here, the largest asymmetry is observed for small U_p, whereas the asymmetry gradually decreases upon increase of U_p. This effect can be as well explained by a domination of the streaking contribution for large U_p, where the broadening of the line due to the larger momentum transfer from the streaking field exceeds the PCI contribution. Again, a similar picture arises in TDSE calculations (cf. Fig. 5).

In a further step, we want to evaluate the asymmetry in more detail. To this end, we introduce a classification parameter ξ, defined as

$$\xi = \frac{|w^- - w^+|}{w^- + w^+}, \tag{53}$$

where $w^\pm$ is the FWHM of the Auger line at $\dot{A} > 0$ and $\dot{A} < 0$, respectively. This parameter $\xi \in [0,1]$ describes the relative asymmetry and is zero for vanishing asymmetry and attains finite positive values smaller than one in any other case.

A. Effect of XUV pump pulse duration

A key property for successful pulse characterization is the existence of observables sensitive to the XUV pulse duration. In Fig. 22 several properties of the Auger line shapes are plotted depending on the XUV pulse duration at fixed $U_p = 100$ meV: the position of the maximum of the line, $\epsilon_m^\pm$, the FWHM of the line, $w^\pm$, and the corresponding asymmetry parameter ξ. Let us first consider the energetic position of the line. For $\dot{A} < 0$, ϵ_m^- is positive, stemming directly from the positive tail of the decay law. For small pulse durations, the forbidden region $\epsilon < \epsilon_0$, discussed in Sec. IV E, is observed with the sharp onset of the line at ϵ_0. With increasing pulse duration, the position of the maximum shifts toward higher energies, a clear consequence of the convolution with the

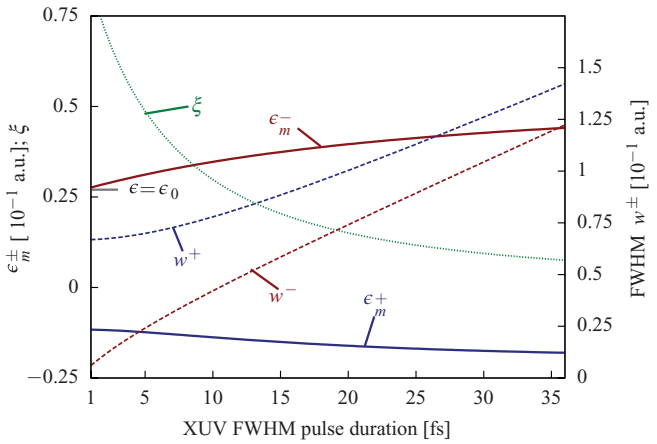

FIG. 22. (Color online) Position of the Auger line's maximum $\epsilon_m^{\pm}$, the corresponding width $w^{\pm}$ and the asymmetry parameter ξ [cf. Eq. (53)] vs XUV pump pulse duration. Data is for Kr *MNN* decay at a ponderomotive potential of 100 meV of the streaking pulse. The forbidden region for $\dot{A}_p < 0$ at infinitesimal short XUV pulse duration is marked by ϵ_0. The superscript "+" ("−") refers to $\dot{A}_p > 0$ ($\dot{A}_p < 0$).

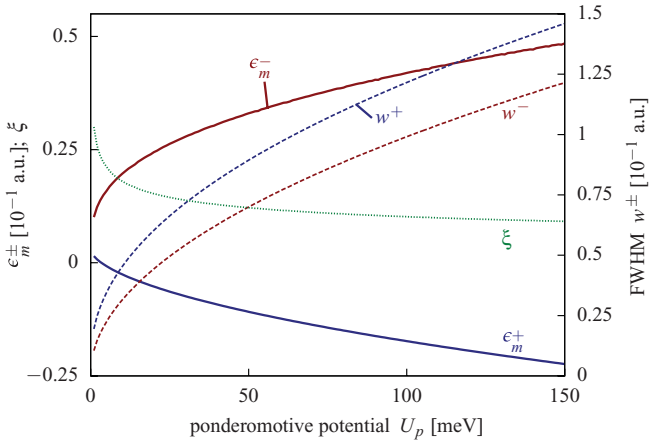

FIG. 23. (Color online) The same as Fig. 22 but for varied ponderomotive potential U_p of the streaking field at a fixed pump pulse duration of 28 fs.

Gaussian-shaped temporal distribution of the XUV pulse. This shift saturates for large pulse durations, $\tau_X \gg \Gamma_A^{-1}$, due to the broad convolution function. For $\dot{A} > 0$ and ϵ_m^+, a similar trend is observed for ϵ_m^+, but with decreasing energy of the maximum. Due to the PCI-induced broadening of the line, the effect is here less pronounced than for the compressed line.

The width of the line, $w^{\pm}$, shows the typical strong influence on the XUV pump pulse duration: The larger the τ_X, the larger is $w^{\pm}$. This phenomenon is the basic principle of the streak camera utilized for the estimation of pulse lengths. Here, the observed asymmetry due to the PCI-induced chirp on the Auger electron's energy manifests itself in two branches for the width: one for $\dot{A} > 0$ labeled by w^+ and one for $\dot{A} < 0$ indicated by w^- (cf. dashed lines in Fig. 22). For conventional chirp-free situations both branches coincide (no asymmetry with respect to $\dot{A} > 0$ and $\dot{A} < 0$).

Since with two opposing detectors, both situations $\dot{A} > 0$ and $\dot{A} < 0$ can be recorded simultaneously, also the asymmetry parameter ξ carries valuable information about the single-shot pulse properties. Its pulse-duration dependence is plotted by the (green) dotted line: For short pulses a large asymmetry of about 0.75 is observed with a rapid decrease down to about 0.1 at pulse durations of 20 fs. The largest variation is found for pulses below 10 fs, where τ_X is comparable to the Auger decay time Γ_A^{-1}. Thus, from measuring the width of the Auger lines at opposite slopes of the streaking vector potential simultaneously, a reconstruction of the pulse duration is possible, even if PCI effects are present.

B. Ponderomotive potential of streaking pulse

An important question is the dependence of the asymmetry on the streaking conditions and, in particular, the ponderomotive potential U_p of the streaking field. This parameter is, in principle, easily tunable in experiments, either through the frequency ω_L (limited by the pulse duration $\tau_X \ll \omega_L^{-1}$) or the intensity E_L^2. In Fig. 23 the position of the maximum, the FWHM, and the asymmetry parameter for a scan of U_p, by variation of E_L, at a fixed XUV pulse duration of 28 fs are shown. For vanishing U_p, no streaking occurs, which gives vanishing energy shifts $\epsilon_m^{\pm}$ and widths $w^{\pm}$. [Note that no natural linewidths are included in Eq. (52).]

For increasing U_p, the position of the maximum of the line shifts toward higher energies for the case of $\dot{A} < 0$ (ϵ_m^-) and toward smaller energies for $\dot{A} > 0$ (ϵ_m^+). This effect is similar to the behavior observed upon variation of τ_X. Also, as in the previous case, two branches of the width can be identified, originating from the asymmetry (dashed lines in Fig. 23). For larger U_p, the momentum transfer from the probing field to the electron increases and, with that, the streaking, resulting in broader lines. Again for the case of chirp-free XUV excitation without PCI effects the "+" and the "−" branches would coincide.

Additionally, the asymmetry parameter ξ is plotted in Fig. 23. Starting from a rather high value at very small U_p, it exhibits a rapid drop when U_p increases to about 10 meV, followed by a slow convergence with only a weak dependence on U_p over a wide range of approximately 100 meV.

Figure 24 summarizes the possibilities for pulse characterization using FA PCI. The asymmetry parameter ξ is shown as a function of τ_X for different U_p of the streaking pulse. For all considered values of U_p a monotonic behavior with large asymmetry for small pulse durations and vice versa is observed. The larger the U_p, the faster is the drop of ξ at small pulse durations and, with the corresponding strong variation with τ_X, a high sensitivity of ξ in the range of pulse durations below 10 to 20 fs occurs. Thus, increasing U_p makes it possible to extend the region of sensitivity to slightly larger XUV pulse durations. In conclusion, measuring ξ at a given ponderomotive potential of the streaking field for $\dot{A} > 0$ and $\dot{A} < 0$ simultaneously utilizing opposite detectors, an estimation of the XUV pulse duration based on (time-resolved) Auger electron spectroscopy is possible. The highest sensitivity is reached for XUV pulse durations below 10 fs with a rather strong variation of the measured parameter ξ by a factor of four.

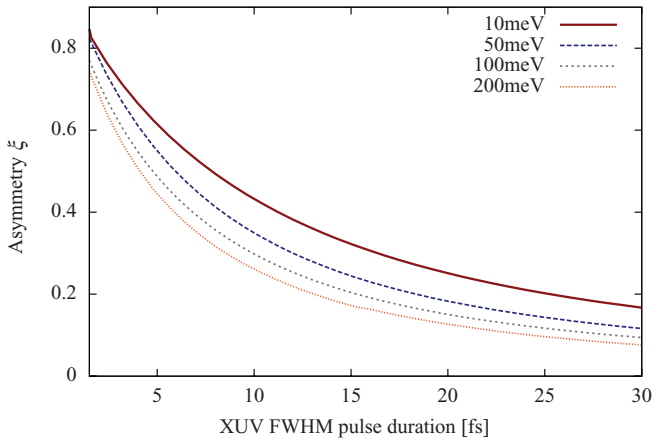

FIG. 24. (Color online) Asymmetry parameter ξ for different ponderomotive potentials of the streaking pulse as a function of the XUV pulse duration. Parameters are the same as for Fig. 22.

VI. CONCLUSIONS AND OUTLOOK

In this paper, we gave a detailed theoretical explanation of the experimental observations in Ref. [20], which show evidence of an energetic chirp in Auger emission. Based on solutions of the TDSE we could reproduce the chirp for model systems and explain its origin by PCI. This formed the basis for classical modeling of the photoelectron and the Auger electron in the continuum, including all electron-electron and electron-ion interactions. Using MC-averaged MD simulations for the electrons, we were able to verify this chirp. The quantitative comparison with experiments including detector resolutions and acceptance geometries using the Xe *NOO* and the Kr *MNN* transitions presented in Ref. [20] shows perfect agreement between our approach and the light-field-driven streak camera in the considered range of parameters. For deeper insight and to obtain a more flexible tool, we derived a classical, analytical line shape model for the Auger electron that fully includes the XUV pulse shape, streaking, and PCI effects and thus captures all important properties. We further showed, how our results may be used as a tool for estimating the length of XUV pump pulses if PCI effects are involved.

In the present work, we focused on the Auger electrons, which was motivated by currently available experiments. The corresponding photoelectron distribution was briefly discussed, and we explained why no energetic chirp is present there. A detailed analysis will be part of a future work. Worthwhile considerations include the influence of additional XUV pulse parameters such as chirp and substructures, for example, spikes as present in the case of free electron laser sources. Additionally, it will be advantageous to extend our purely classical model for the FA PCI line shape to account for quantum effects in order to describe interference and spin effects.

Finally, it would be very interesting to investigate in experiments with either Kr *MNN* or Xe *NOO* the behavior when the XUV photon energy is increased. If the proposed FA PCI scenario is correct, then the chirp of the Auger spectra should vanish when the photoelectron energy starts to exceed the Auger electron energy.

ACKNOWLEDGMENTS

We thank B. Schütte, U. Frühling, and M. Drescher for many interesting discussions of their experiments. We are grateful to N. Kabachnik for bringing to our attention the early work on PCI, in particular Ref. [23]. This work has been supported by the BMBF-Verbund "FLASH" and Grant No. shp0006 for computer time at HLRN.

[1] T. Brabec and F. Krausz, Rev. Mod. Phys. **72**, 545 (2000).
[2] P. Agostini and L. F. DiMauro, Rep. Prog. Phys. **67**, 813 (2004).
[3] A. Scrinzi, M. Y. Ivanov, R. Kienberger, and D. M. Villeneuve, J. Phys. B **39**, R1 (2006).
[4] F. Krausz and M. Ivanov, Rev. Mod. Phys. **81**, 163 (2009).
[5] E. Goulielmakis, M. Uiberacker, R. Kienberger, A. Baltuska, V. Yakovlev, A. Scrinzi, T. Westerwalbesloh, U. Kleineberg, U. Heinzmann, M. Drescher, and F. Krausz, Science **305**, 1267 (2004).
[6] M. Uiberacker, T. Uphues, M. Schultze, A. J. Verhoef, V. Yakovlev, M. F. Kling, J. Rauschenberger, N. M. Kabachnik, H. Schröder, M. Lezius, K. L. Kompa, H. Muller, M. J. J. Vrakking, S. Hendel, U. Kleineberg, U. Heinzmann, M. Drescher, and F. Krausz, Nature (London) **446**, 627 (2007).
[7] M. Drescher, M. Hentschel, R. Kienberger, M. Uiberacker, V. Yakovlev, A. Scrinzi, T. Westerwalbesloh, U. Kleineberg, U. Heinzmann, and F. Krausz, Nature (London) **419**, 803 (2002).
[8] M. Schultze *et al.*, Science **328**, 1658 (2010).
[9] C. Wheatstone, Philos. Trans. R. Soc. London **124**, 583 (1834).
[10] D. J. Bradley, B. Liddy, and W. Sleat, Opt. Commun. **2**, 391 (1971).
[11] J. Feng, H. J. Shin, J. R. Nasiatka, W. Wan, A. T. Young, G. Huang, A. Comin, J. Byrd, and H. A. Padmore, Appl. Phys. Lett. **91**, 134102 (2007).
[12] R. Kienberger, E. Goulielmakis, M. Uiberacker, A. Baltuska, V. Yakovlev, F. Bammer, A. Scrinzi, T. Westerwalbesloh, U. Kleineberg, U. Heinzmann, M. Drescher, and F. Krausz, Nature (London) **427**, 817 (2004).
[13] J. Itatani, F. Quéré, G. L. Yudin, M. Y. Ivanov, F. Krausz, and P. B. Corkum, Phys. Rev. Lett. **88**, 173903 (2002).
[14] A. Ipp, J. Evers, C. H. Keitel, and K. Z. Hatsagortsyan, Phys. Lett. B **702**, 383 (2011).
[15] U. Frühling, M. Wieland, M. Gensch, T. Gebert, B. Schütte, M. Krikunova, R. Kalms, F. Budzyn, O. Grimm, J. Rossbach, E. Plönjes, and M. Drescher, Nat. Photonics **3**, 523 (2009).
[16] E. E. Krasovskii and M. Bonitz, Phys. Rev. Lett. **99**, 247601 (2007).
[17] E. E. Krasovskii and M. Bonitz, Phys. Rev. A **80**, 053421 (2009).
[18] L. Meitner, Z. Phys. **11**, 35 (1922).
[19] P. Auger, Comptes Rendus **180**, 65 (1925).

[20] B. Schütte, S. Bauch, U. Frühling, M. Wieland, M. Gensch, E. Plönjes, T. Gaumnitz, A. Azima, M. Bonitz, and M. Drescher, Phys. Rev. Lett. (in press).
[21] B. Schütte, U. Frühling, M. Wieland, A. Azima, and M. Drescher, Opt. Express **19**, 18833 (2011).
[22] A. Niehaus, J. Phys. B **10**, 1845 (1977).
[23] G. N. Ogurtsov, J. Phys. B **16**, L745 (1983).
[24] A. Russek and W. Mehlhorn, J. Phys. B **19**, 911 (1986).
[25] M. Y. Kuchiev and S. A. Sheinermann, Sov. Phys. JETP **63**, 986 (1986) [Zh. Eksp. Teor. Fiz. **90**, 1680 (1986)].
[26] M. Y. Kuchiev and S. A. Sheinerman, Usp. Fiz. Nauk **158**, 353 (1989) [Sov. Phys. Usp. **32**, 569 (1989)].
[27] T. Åberg, Phys. Scr. T **41**, 71 (1992).
[28] S. L. Haan, R. Grobe, and J. H. Eberly, Phys. Rev. A **50**, 378 (1994).
[29] S. X. Hu and L. A. Collins, Phys. Rev. A **71**, 062707 (2005).
[30] U. Fano, Phys. Rev. **124**, 1866 (1961).
[31] A. K. Kazansky and N. M. Kabachnik, Phy. Rev. A **72**, 052714 (2005).
[32] A. K. Kazansky and N. M. Kabachnik, Phys. Rev. A **73**, 062712 (2006).
[33] A. K. Kazansky, I. P. Sazhina, and N. M. Kabachnik, J. Phys. B **42**, 245601 (2009).
[34] C. Buth and K. J. Schafer, Phys. Rev. A **80**, 033410 (2009).
[35] M. Wickenhauser and J. Burgdörfer, Laser Phys. **14**, 492 (2004).
[36] M. Wickenhauser, J. Burgdörfer, F. Krausz, and M. Drescher, Phys. Rev. Lett. **94**, 023002 (2005).
[37] U. Hergenhahn, A. De Fanis, G. Prümper, A. K. Kazansky, N. M. Kabachnik, and K. Ueda, Phys. Rev. A **73**, 022709 (2006).
[38] U. Hergenhahn, A. De Fanis, G. Prümper, A. K. Kazansky, N. M. Kabachnik, and K. Ueda, J. Phys. B **38**, 2843 (2005).
[39] A. K. Kazansky and N. M. Kabachnik, J. Phys. B **42**, 121002 (2009).
[40] A. K. Kazansky and N. M. Kabachnik, J. Phys. B **43**, 035601 (2010).
[41] Q. Su and J. H. Eberly, Phys. Rev. A **44**, 5997 (1991).
[42] S. Bauch, K. Balzer, and M. Bonitz, Europhys. Lett. **91**, 53001 (2010).
[43] T. N. Rescigno and C. W. McCurdy, Phys. Rev. A **62**, 032706 (2000).
[44] B. I. Schneider, L. A. Collins, and S. X. Hu, Phys. Rev. E **73**, 036708 (2006).
[45] G. Snell, E. Kukk, B. Langer, and N. Berrah, Phys. Rev. A **61**, 042709 (2000).
[46] E. W. Weisstein, From MathWorld—A Wolfram Web Resource (2011) [http://mathworld.wolfram.com/SpherePointPicking.html].
[47] T. Ott, P. Ludwig, H. Kählert, and M. Bonitz, in *Introduction to complex plasmas* edited by M. Bonitz, N. Horing, and P. Ludwig, Springer Series in Atomic, Optical and Plasma Physics, Vol. 59 (Springer, Berlin, 2010).